Supporting Information for "Geophysical imaging of the deep critical zone architecture reveals the complex interplay between hydrological and weathering processes in a volcanic tropical catchment"

S. Pasquet[1], J. Marçais[2], J. L. Hayes[3], P. Sak[3,4], L. Ma[5] and J. Gaillardet[1]

[1]Université de Paris, Institut de physique du globe de Paris, CNRS, Paris, France

[2]INRAE, UR RiverLy, Villeurbanne, France

[3]Department of Earth Sciences, Dickinson College, Carlisle PA, USA

[4]Earth and Environmental Systems Institute and Department of Geosciences, Pennsylvania State University, University Park, PA, USA

[5]University of Texas at El Paso, El Paso TX, USA

Contents of this file

Introduction

Here we provide additional figures aimed at validating the processing, inversion and interpolation steps described in the main manuscript. We specifically give more details about the seismic acquisition, the SRT and MASW workflows, and give a complete description of the petrophysical model and its calibration procedure. We finally describe the average kriging procedure used to interpolate weathering front and water table depths.

S1. Seismic Data Acquisition

For both acquisition campaigns, we used 14-Hz vertical-component geophones, spaced at 4 m in 2016, and at 2 m in 2019. Shots were recorded every 10 m with a 5.4-kg sledgehammer swung onto a hard plate. For each shot, the sampling rate was 0.125 ms and the recording time was 850 ms in order to include the full seismic wavefield. Start and end points of each profile were recorded with a handheld GPS and relative elevations at each geophone location were measured using a laser rangefinder.

S2. Seismic Refraction Tomography

Tomographic inversions are performed in pyGIMLi (Rücker et al., 2017), where the inversion domain is parameterized with a 2D mesh of constant velocity tetrahedrons. Rays are traced through the mesh using a shortest path algorithm (Dijkstra, 1959; Moser, 1991) and updates are found by solving a regularized, linear inverse problem. We used 144 combinations of starting models and regularization parameters (Table S1) in order to explore the non-uniqueness of the inversion and estimate the uncertainty of the velocity distribution along each profile. A selection is then applied to keep only the inversions performed with a set of parameters that obtained a root mean square error < 2.5 ms and

a $\chi^2 < 2$ for all the profiles. The selected models are then merged to create an average velocity model and its associated uncertainty. Models are masked at depth below the lowest raypath (Figure S1). The standard deviations along each profile are computed to estimate how the velocity likelihood varies laterally and at depth (Figure S2).

S3. Multichannel Analysis of Surface-wave

The seismic data were processed to perform surface-wave dispersion inversion and profiling (Pasquet & Bodet, 2017) using the SWIP software package (available at `https://github.com/SWIPdev/SWIP/releases`). SWIP uses windowing and stacking techniques (Neducza, 2007; O'Neill et al., 2003) to take advantage of redundant seismic data and retrieve a 2D model of V_S from a succession of 1D inversions. Dispersion images were extracted every 2 m along each profile with the novel multiwindow weighted stacking of surface-wave procedure (Pasquet et al., 2020), using a set of 6 windows with evenly spaced apertures ranging between 14 m and 94 m. For each window along the profile, dispersion images were computed for each aperture using all shots located between 4 and 20 m away from the windowed data subset. All 6 individual dispersion images were then stacked as one final image with increased signal to noise ratio, doing so every 2 m along the seismic profile. Dispersion curves are eventually identified and picked on each of the stacked images to characterize the lateral variability of the phase velocity vs frequency relationship.

Dispersion curves are then inverted with the neighborhood algorithm (NA) developed in (Sambridge, 1999) and implemented for subsurface applications within the open software package Geopsy (Wathelet et al., 2004). The NA carries out a random search

within a pre-defined parameter space, i.e. V_P, V_S, density and thickness of each layer. In Geopsy, theoretical dispersion curves are computed from the elastic parameters using the Thomson-Haskell matrix propagator technique (Haskell, 1953; Thomson, 1950) as implemented in (Dunkin, 1965). We set the inversion parameterization as a stack of ten layers overlaying a half-space in order to correctly describe smooth velocity gradients encountered in such weathered materials. The thickness of each layer was set to be bound between 0.5 and 1.5 m in the upper layer, these limits then exponentially increasing in the following layers until reaching 1.5 and 6 m in the deepest layer. The valid parameter range for sampling velocity models was 10 to 2500 m/s for V_S, with velocities constrained to only increase with depth, while V_P was automatically parameterized from SRT results.

For each 1D inversion, models matching the observed data within the error bars are selected to build a misfit-weighted final model. After checking phase velocity residuals (Figure S3), the depth of investigation (DOI) is estimated from the standard deviation of all selected models, using a threshold of 15% on the standard deviation to determine the DOI and limit the extent of the V_S model (Figure S4). Each 1D V_S model is finally represented at its corresponding extraction position to create a 2D V_S section. We eventually compared observed and calculated phase velocity for each window position, and computed their residuals to check the quality of the inversion.

S4. Petrophysical inversion

In order to estimate porosity and saturation from V_P and V_S, we used a petrophysical model based on the Hertz-Mindlin contact theory. We followed the strategy presented by (Pasquet et al., 2016) and applied in an hydrothermal system in Yellowstone. The model

is used to calculate bulk elastic parameters of the medium so as to simulate realistic values of V_P and V_S that can be compared to those measured with SRT and MASW. With this model, we represent the medium as an aggregate of randomly packed spheres and simulate their bulk elastic properties (i.e. bulk and shear modulus) as functions of the elastic properties of constituent minerals, porosity, saturation, and several model parameters.

We assumed a unique mineralogical composition in the grain following the description by Buss et al. (2010) (66% clay, 28% hydroxides and 6% quartz). For each mineral compound, we use the elastic parameters found in the literature and summarized in Table S2. The elastic parameters (K_g and G_g) of the grains are then computed from this mineralogical composition with the Voigt-Reuss-Hill average (Hill, 1952; Mavko et al., 2003):

$$(K_g, G_g) = \frac{1}{2}\left[\sum_{i=1}^{m} f_i(K_i, G_i) + \left(\sum_{i=1}^{m} \frac{f_i}{(K_i, G_i)}\right)^{-1}\right], \tag{1}$$

where m is the number of mineral constituents, f_i is the volumetric fraction of the i-th constituent of the solid phase, and K_i and G_i are the bulk and shear moduli of the i-th constituent, respectively. From K_g and G_g, we can compute the Poisson's ratio ν_g of the grains:

$$\nu_g = \frac{1}{2}\left(\frac{3K_g - 2G_g}{3K_g + G_g}\right), \tag{2}$$

while their density ρ_g is calculated following:

$$\rho_g = \sum_{i=1}^{m} f_i \rho_i. \tag{3}$$

The bulk density of the medium (ρ_b) can then be calculated for different combinations of porosity (Φ) and saturation (W) with the following equation:

$$\rho_b = \Phi(W\rho_w + (1-W)\rho_a) + (1-\Phi)\rho_g, \tag{4}$$

where ρ_w and ρ_a are the densities of water and air, respectively.

At this point we can compute the bulk elastic parameters of the dry rock frame made of a random pack of identical spherical grains subject to a hydrostatic pressure P_{eff}. The bulk modulus K_{HM} is computed as follow:

$$K_{HM} = \left[\frac{n^2(1-\Phi_c)^2 G_g^2}{18\pi^2(1-\nu_g)^2} P_{eff}\right]^{\frac{1}{3}}, \tag{5}$$

where n is the average number of contacts between grains and Φ_c a critical porosity over which the medium changes from a suspension to a grain-supported material. As recommended by Nur, Mavko, Dvorkin, and Galmudi (1998), we used a critical porosity of 0.36. Since the traditional Hertz-Mindlin formulation tends to overestimate shear-wave velocities in unconsolidated media (Bachrach & Avseth, 2008), we use the approach proposed by Mavko et al. (2003) to calculate the shear modulus (G_{HM}). This approach allows a fraction f of the grain contacts to be frictionless, the rest having perfect adhesion:

$$G_{HM} = \frac{2+3f-(1+3f)\nu_g}{5(2-\nu_g)} \left[\frac{3n^2(1-\Phi_c)^2 G_g^2}{2\pi^2(1-\nu_g)^2} P_{eff}\right]^{\frac{1}{3}}, \tag{6}$$

In the case of full saturation, P_{eff} is calculated as follow:

$$P_{eff} = (\rho_b - \rho_w) g D, \tag{7}$$

where g is the gravitational acceleration and D is the depth below ground level. In partially saturated media, P_{eff} is calculated as:

$$P_{eff} = \rho_b g D. \tag{8}$$

For porosity Φ higher than Φ_c, the effective bulk (K_{dry}) and shear (G_{dry}) moduli of the dry frame are calculated with the modified upper Hashin-Shtrikman (H-S) bound (Dvorkin et al., 1999):

$$K_{dry} = \left[\frac{\frac{1-\Phi}{1-\Phi_c}}{K_{HM} + \frac{4}{3}G_{HM}} + \frac{\frac{\Phi-\Phi_c}{1-\Phi_c}}{\frac{4}{3}G_{HM}} \right]^{-1} - \frac{4}{3}G_{HM}, \tag{9}$$

$$G_{dry} = \left[\frac{\frac{1-\Phi}{1-\Phi_c}}{G_{HM} + Z} + \frac{\frac{\Phi-\Phi_c}{1-\Phi_c}}{Z} \right]^{-1} - Z. \tag{10}$$

For porosity Φ lower than Φ_c, K_{dry} and G_{dry} are calculated with the modified lower H-S bound:

$$K_{dry} = \left[\frac{\frac{\Phi}{\Phi_c}}{K_{HM} + \frac{4}{3}G_{HM}} + \frac{1 - \frac{\Phi}{\Phi_c}}{K_g + \frac{4}{3}G_{HM}} \right]^{-1} - \frac{4}{3}G_{HM}, \tag{11}$$

$$G_{dry} = \left[\frac{\frac{\Phi}{\Phi_c}}{G_{HM} + Z} + \frac{1 - \frac{\Phi}{\Phi_c}}{G_g + Z} \right]^{-1} - Z. \tag{12}$$

In both cases, Z is defined as follow:

$$Z = \frac{G_{HM}}{6} \left(\frac{9K_{HM} + 8G_{HM}}{K_{HM} + 2G_{HM}} \right). \tag{13}$$

We then use Gassmann fluid substitution equations (Gassmann, 1951; Mavko et al., 2003) to estimate the effective bulk (K_{sat}) modulus in partial saturation conditions:

$$K_{sat} = K_G \frac{\Phi K_{dry} - (1+\Phi)\frac{K_{fl}K_{dry}}{K_G} + K_{fl}}{(1-\Phi)K_{fl} + \Phi K_G - \frac{K_{fl}K_{dry}}{K_G}}, \tag{14}$$

where K_{fl} is the effective bulk modulus of the fluid and is defined with the Brie's fluid mixing equation (Brie et al., 1995; Wollner & Dvorkin, 2018):

$$K_{fl} = W^e(K_w - K_a) + K_a. \tag{15}$$

The empirical constant e can range between 1 and ∞. In full or partial saturation conditions, the effective shear modulus G_{sat} is identical to the dry effective shear modulus G_{dry}.

Once the effective elastic moduli and density in partial saturation conditions are known, the elastic wave velocities can be calculated as follow:

$$V_P = \sqrt{\frac{K_{sat} + \frac{4}{3}G_{sat}}{\rho_b}} \tag{16}$$

$$V_S = \sqrt{\frac{G_{sat}}{\rho_b}} \tag{17}$$

We performed a preliminary grid search to find the best set of model parameters n, f and e. n ranged between 5 and 20 with steps of 1, f between 0 and 1 with steps of 0.1, and e between 1 and 40 with steps of 1. We minimized a misfit function that incorporates both density and saturation constraints in control points along profile P5. On the one hand, we compare the estimated bulk density in the upper 10 m at the end of P5 ($X = 170$ m; green star in Figure 2 in the main manuscript) with the average density (1000 kg/m^3) measured in a direct sample nearby (Buss et al., 2010). On the other hand, we compare the saturation value estimated in the stream along P5 close to the surface to its expected value $W = 1$ (we expect full saturation there since water was flowing in the stream at the time of the measurements). By minimizing both density and saturation differences, we were eventually able to define the best parameters as $n = 17$, $f = 0.9$ and $e = 24$ (Figure S5) and used them to estimate porosity and saturation along all profiles.

The grid search inversion was then performed on each geophysical profile on cells containing both V_P and V_S information. Porosity and saturation ranged from 0 to 1, with

100 samples following a logarithmic distribution to better sample the strong velocity gradient at high saturation and low porosity. The root-mean-square errors of each profile are summarized in Figure S6. Water saturation uncertainties estimated with the grid search inversions (Figure S8) are low (¡5%), especially in the water-saturated areas of the subsurface, thus reinforcing our confidence in the interpreted water table levels. Porosity uncertainties Figure S8) are also high (about 8% on average), yet they still allow to draw valid interpretations about porosity variations between the main areas of the catchment.

S5. Kriging interpolation

Kriging consists of estimating the unknown value of a variable (i.e., the depth or the elevation) at any point in space using a weighted average of all available observations. The weights given to each data points are based on the spatial correlations and trends that exist within the data set, and also depend on the distance from data points. We first computed an experimental variogram of the data which represents the semivariance (i.e., the average difference of all pairs of data points separated by the same distance) as a function of the distance between these points. A theoretical variogram was then adjusted to fit the experimental variogram in order to describe the data semivariance with a mathematical expression for any distance between points. A more detailed description of the kriging method can be found in Oliver and Webster (2014) and in geostatistics textbooks (e.g., Chilès & Delfiner, 2009).

We followed a four-step procedure to interpolate elevation data of both the water table and the weathering front. This procedure consists in: (i) removing the quadratic trend of the elevation data, (ii) compute the experimental variogram, (iii) test several theo-

retical variograms, and (iv) apply the best fitting variogram (Oliver & Webster, 2014). We eventually used the super-spherical model (Matern, 1986) as it provided the best fit with experimental variograms of elevation data for both weathering front and water table interpolations (Figure S9). A similar procedure was used to interpolate depth data, with a first step consisting in converting elevation data into depth data by substracting weathering front and water table elevation to the landscape surface topography extracted from the digital elevation model (DEM). We then used ordinary kriging to estimate detrended elevations and depths of both the weathering front and the water table along a regular grid of 10x10 m cells covering the entire watershed. We eventually added the quadratic trend back to the kriged elevations, and the surface elevations back to the kriged depths, so as to obtain two distinct elevation interpolations for both the weathering front and the water table. Following the average kriging methodology proposed by Snyder (2008), we then averaged the results of both interpolations to produce reliable estimates of weathering front and water table elevations in the Quiock watershed (Figure S10). We eventually computed the depth of each interface by removing the landscape surface topography to the interpolated elevations.

References

Bachrach, R., & Avseth, P. (2008, November). Rock physics modeling of unconsolidated sands: Accounting for nonuniform contacts and heterogeneous stress fields in the effective media approximation with applications to hydrocarbon exploration. *Geophysics*, *73*(6), E197–E209. Retrieved from `http://library.seg.org/doi/abs/10.1190/1.2985821` doi: 10.1190/1.2985821

Brie, A., Pampuri, F., Marsala, A. F., & Meazza, O. (1995, October). Shear Sonic Interpretation in Gas-Bearing Sands. OnePetro. Retrieved from https://onepetro.org/SPEATCE/proceedings/95SPE/All-95SPE/SPE-30595-MS/57668 doi: 10.2118/30595-MS

Buss, H. L., White, A. F., Dessert, C., Gaillardet, J., Blum, A. E., & Sak, P. B. (2010). Depth profiles in a tropical, volcanic critical zone observatory: Basse-Terre, Guadeloupe. In *Water-Rock Interaction - Proceedings of the 13th International Conference on Water-Rock Interaction, WRI-13* (pp. 245–248). Retrieved from https://pennstate.pure.elsevier.com/en/publications/depth-profiles-in-a-tropical-volcanic-critical-zone-observatory-b

Chicot, D., Mendoza, J., Zaoui, A., Louis, G., Lepingle, V., Roudet, F., & Lesage, J. (2011, October). Mechanical properties of magnetite (Fe3O4), hematite (α-Fe2O3) and goethite (α-FeO·OH) by instrumented indentation and molecular dynamics analysis. *Materials Chemistry and Physics*, *129*(3), 862–870. Retrieved from http://www.sciencedirect.com/science/article/pii/S0254058411004627 doi: 10.1016/j.matchemphys.2011.05.056

Chilès, J.-P., & Delfiner, P. (2009). *Geostatistics: Modeling Spatial Uncertainty*. John Wiley & Sons. (Google-Books-ID: tZl07WdjYHgC)

Dijkstra, E. W. (1959). A Note on Two Problems in Connexion with Graphs. *Numerische Mathematik*, *1*, 269–271. Retrieved from https://eudml.org/doc/131436

Dunkin, J. W. (1965, January). Computation of modal solutions in layered, elastic media at high frequencies. *Bulletin of the Seismological Society of America*, *55*(2), 335–358.

Retrieved from http://www.bssaonline.org/content/55/2/335

Dvorkin, J., Prasad, M., Sakai, A., & Lavoie, D. (1999). Elasticity of marine sediments: Rock physics modeling. *Geophysical Research Letters*, *26*, 1781–1784. Retrieved from http://adsabs.harvard.edu/abs/1999GeoRL..26.1781D doi: 10.1029/1999GL900332

Gassmann, F. (1951, October). Elastic waves through a packing of spheres. *Geophysics*, *16*(4), 673–685. Retrieved from http://library.seg.org/doi/abs/10.1190/1.1437718 doi: 10.1190/1.1437718

Haskell, N. A. (1953, January). The dispersion of surface waves on multilayered media. *Bulletin of the Seismological Society of America*, *43*(1), 17–34. Retrieved from http://bssa.geoscienceworld.org/content/43/1/17

Hill, R. (1952). The Elastic Behaviour of a Crystalline Aggregate. *Proceedings of the Physical Society. Section A*, *65*(5), 349. Retrieved from http://stacks.iop.org/0370-1298/65/i=5/a=307 doi: 10.1088/0370-1298/65/5/307

Matern, B. (1986). *Spatial Variation* (2nd ed.). New York: Springer-Verlag. Retrieved from https://www.springer.com/gp/book/9781461578925 doi: 10.1007/978-1-4615-7892-5

Mavko, G., Mukerji, T., & Dvorkin, J. (2003). *The Rock Physics Handbook: Tools for Seismic Analysis of Porous Media* (2nd ed.). Cambridge University Press.

Moser, T. (1991, January). Shortest path calculation of seismic rays. *Geophysics*, *56*(1), 59–67. Retrieved from http://library.seg.org/doi/abs/10.1190/1.1442958 doi: 10.1190/1.1442958

Neducza, B. (2007). Stacking of surface waves. *Geophysics*, *72*(2), 51–58. Retrieved from http://link.aip.org/link/?GPY/72/V51/1 doi: 10.1190/1.2431635

Nur, A., Mavko, G., Dvorkin, J., & Galmudi, D. (1998, March). Critical porosity: A key to relating physical properties to porosity in rocks. *The Leading Edge*, *17*(3), 357–362. Retrieved from http://library.seg.org/doi/abs/10.1190/1.1437977 doi: 10.1190/1.1437977

Oliver, M. A., & Webster, R. (2014, February). A tutorial guide to geostatistics: Computing and modelling variograms and kriging. *CATENA*, *113*, 56–69. Retrieved from https://www.sciencedirect.com/science/article/pii/S0341816213002385 doi: 10.1016/j.catena.2013.09.006

O'Neill, A., Dentith, M., & List, R. (2003, January). Full-waveform P-SV reflectivity inversion of surface waves for shallow engineering applications. *Exploration Geophysics*, *34*(3), 158–173. Retrieved from http://www.publish.csiro.au/paper/EG03158

Pasquet, S., & Bodet, L. (2017, July). SWIP: An integrated workflow for surface-wave dispersion inversion and profiling. *Geophysics*, *82*(6), WB47–WB61. Retrieved from http://library.seg.org/doi/abs/10.1190/geo2016-0625.1 doi: 10.1190/geo2016-0625.1

Pasquet, S., Holbrook, W. S., Carr, B. J., & Sims, K. W. W. (2016, December). Geophysical imaging of shallow degassing in a Yellowstone hydrothermal system. *Geophysical Research Letters*, *43*(23), 2016GL071306. Retrieved from http://onlinelibrary.wiley.com/doi/10.1002/2016GL071306/abstract doi: 10.1002/2016GL071306

Pasquet, S., Wang, W., Chen, P., & Flinchum, B. A. (2020, December). Multi-window weighted stacking of surface-wave dispersion. *Geophysics*, *86*(2), EN39–EN50. Retrieved from https://library.seg.org/doi/full/10.1190/geo2020-0096.1 (Publisher: Society of Exploration Geophysicists) doi: 10.1190/geo2020-0096.1

Rücker, C., Günther, T., & Wagner, F. M. (2017, December). pyGIMLi: An open-source library for modelling and inversion in geophysics. *Computers & Geosciences*, *109*, 106–123. Retrieved from http://www.sciencedirect.com/science/article/pii/S0098300417300584 doi: 10.1016/j.cageo.2017.07.011

Sambridge, M. (1999). Geophysical inversion with a neighbourhood algorithm—I. Searching a parameter space. *Geophysical Journal International*, *138*(2), 479–494. Retrieved from http://onlinelibrary.wiley.com/doi/10.1046/j.1365-246X.1999.00876.x/abstract doi: 10.1046/j.1365-246X.1999.00876.x

Snyder, D. T. (2008). Estimated Depth to Ground Water and Configuration of the Water Table in the Portland, Oregon Area.
doi: 10.3133/SIR20085059

Thomson, W. T. (1950, February). Transmission of elastic waves through a stratified solid medium. *Journal of Applied Physics*, *21*(2), 89–93. Retrieved from http://jap.aip.org/resource/1/japiau/v21/i2/p89_s1 doi: doi:10.1063/1.1699629

Wathelet, M., Jongmans, D., & Ohrnberger, M. (2004, November). Surface-wave inversion using a direct search algorithm and its application to ambient vibration measurements. *Near Surface Geophysics*, *2*(4), 211–221. Retrieved from http://

earthdoc.eage.org/detail.php?pubid=8129 doi: 10.3997/1873-0604.2004018

Wollner, U., & Dvorkin, J. (2018). Effective bulk modulus of the pore fluid at patchy saturation. *Geophysical Prospecting*, *66*(7), 1372–1383. Retrieved from http://onlinelibrary.wiley.com/doi/abs/10.1111/1365-2478.12632 (_eprint: https://onlinelibrary.wiley.com/doi/pdf/10.1111/1365-2478.12632) doi: 10.1111/1365-2478.12632

Table S1. Regularization parameters for seismic refraction tomography inversions.

V_{top} (m/s)	V_{bottom} (m/s)	z_{weight}	$lambda$
250	2000	0.25	2
500	3000	0.5	20
750	4000	0.75	200
	5000	1	

Table S2. Elastic parameters for the different minerals found in the regolith

	$K_{mineral}$ (GPa)	$G_{mineral}$ (GPa)	$\rho_{mineral}$ (kg/m^3)
Clays (Mavko et al., 2003)	1.5	1.4	1580
Hydroxides (Chicot et al., 2011)	200	50	5000
Quartz (Mavko et al., 2003)	37	44	2650

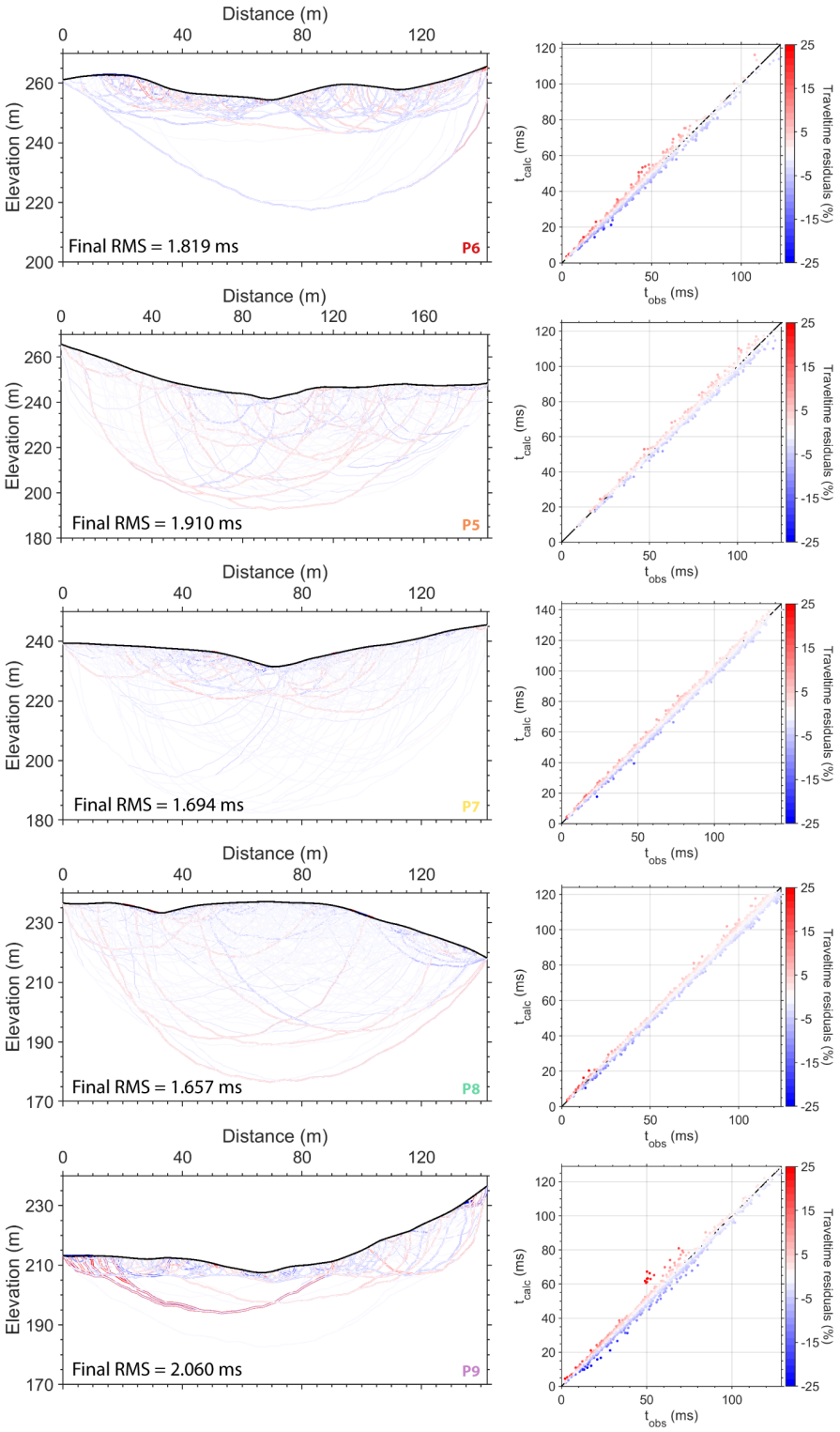

Figure S1. Left column: Raypath distribution for each seismic profile used to mask final V_P models. Right column: Observed vs Calculated traveltimes. The colorscale in both columns corresponds to traveltime residuals (in %).

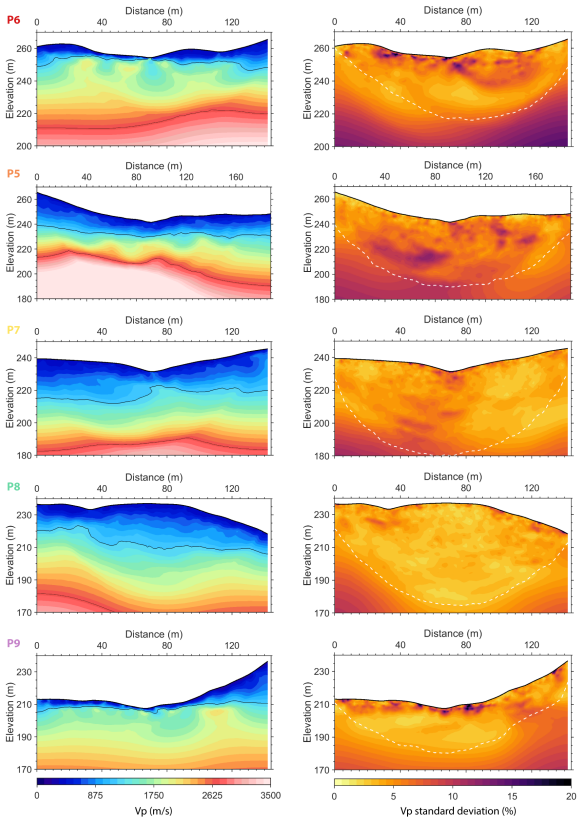

Figure S2. Standard deviation of V_P (in %) computed for each profile from the results of 144 inversions. The white dashed line corresponds to the DOI, estimated from the maximum depth of raypaths (cf Figure S1).

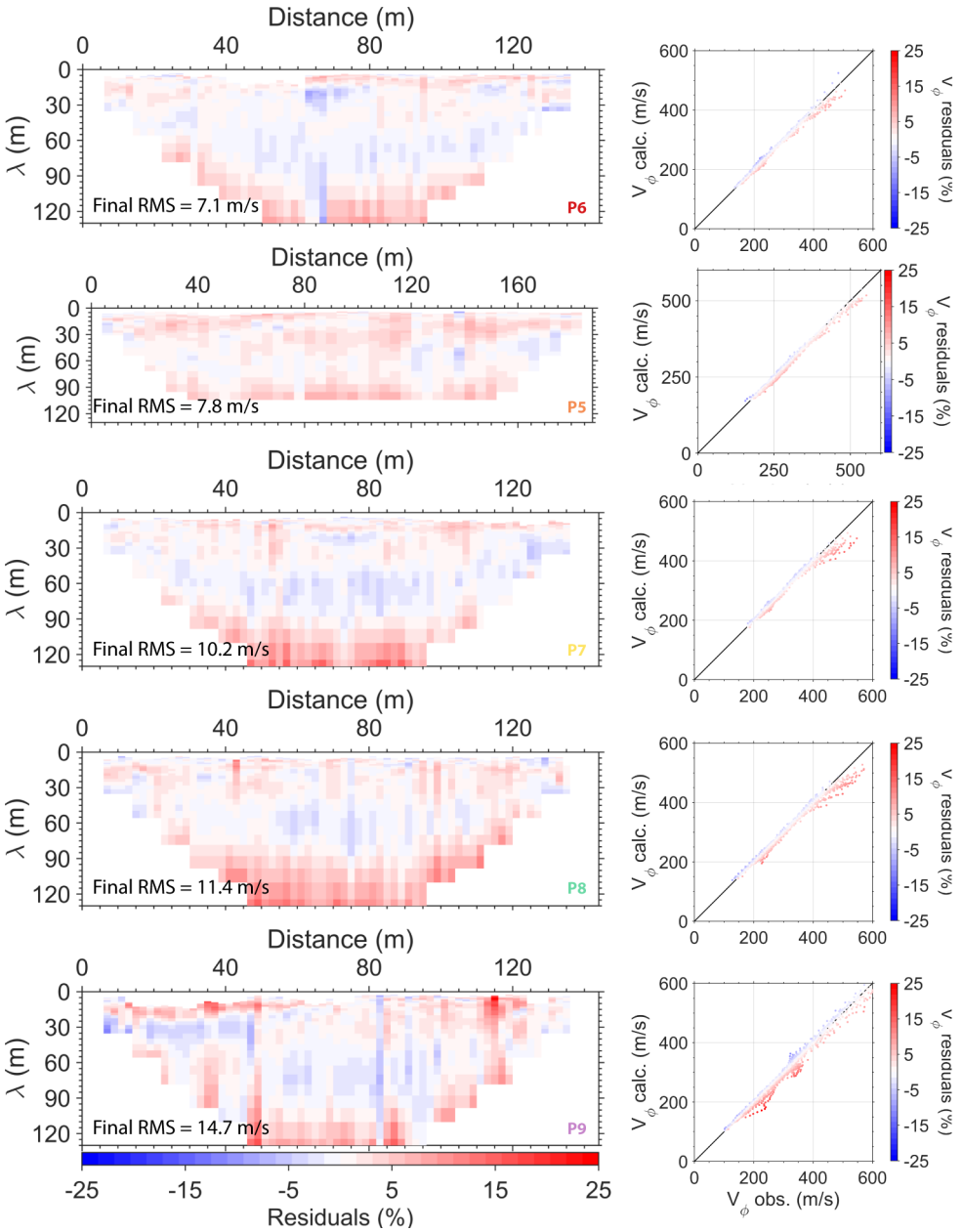

Figure S3. Left column: Phase velocity residuals for each seismic profile. Right column: Observed vs Calculated phase velocities. The colorscale in both columns corresponds to phase velocity residuals (in %).

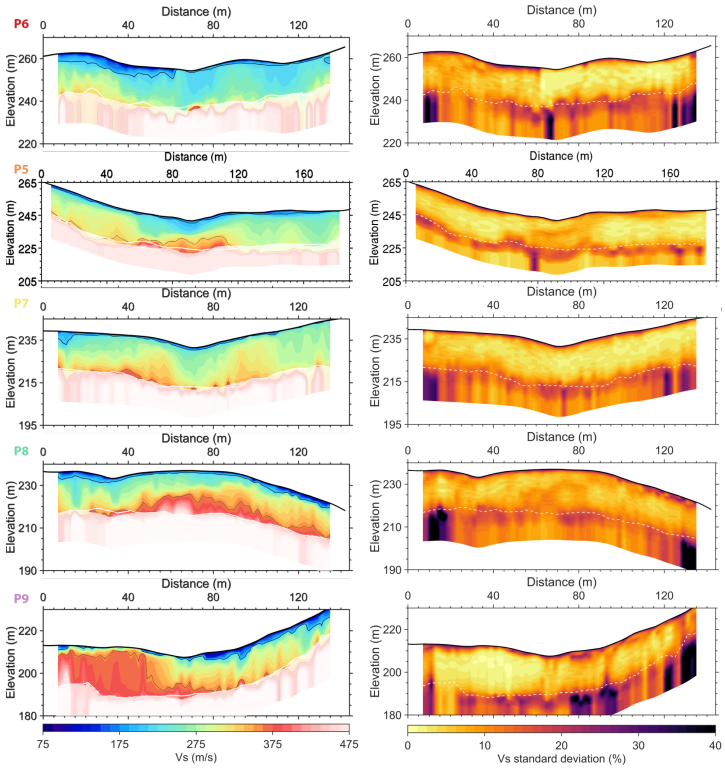

Figure S4. Standard deviation of V_S (in %) computed for each profile from the results of NA inversions. The white dashed line corresponds to the DOI, estimated with a threshold of 15% on the standard deviation.

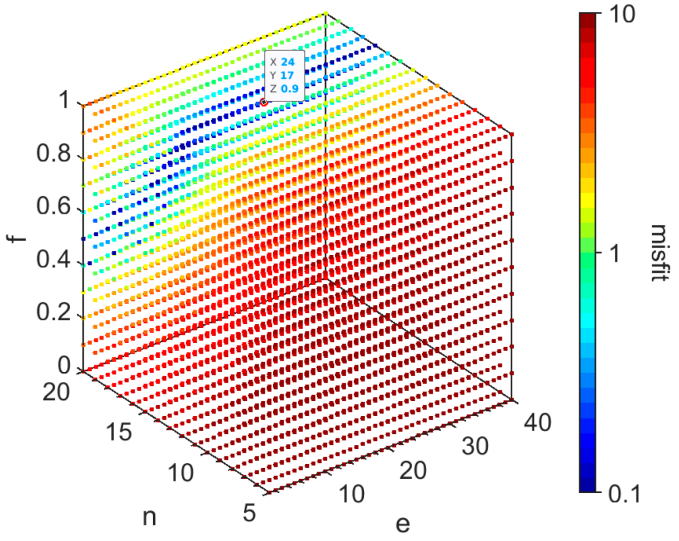

Figure S5. Results of the grid search inversion to determine best parameters for n, f and e.

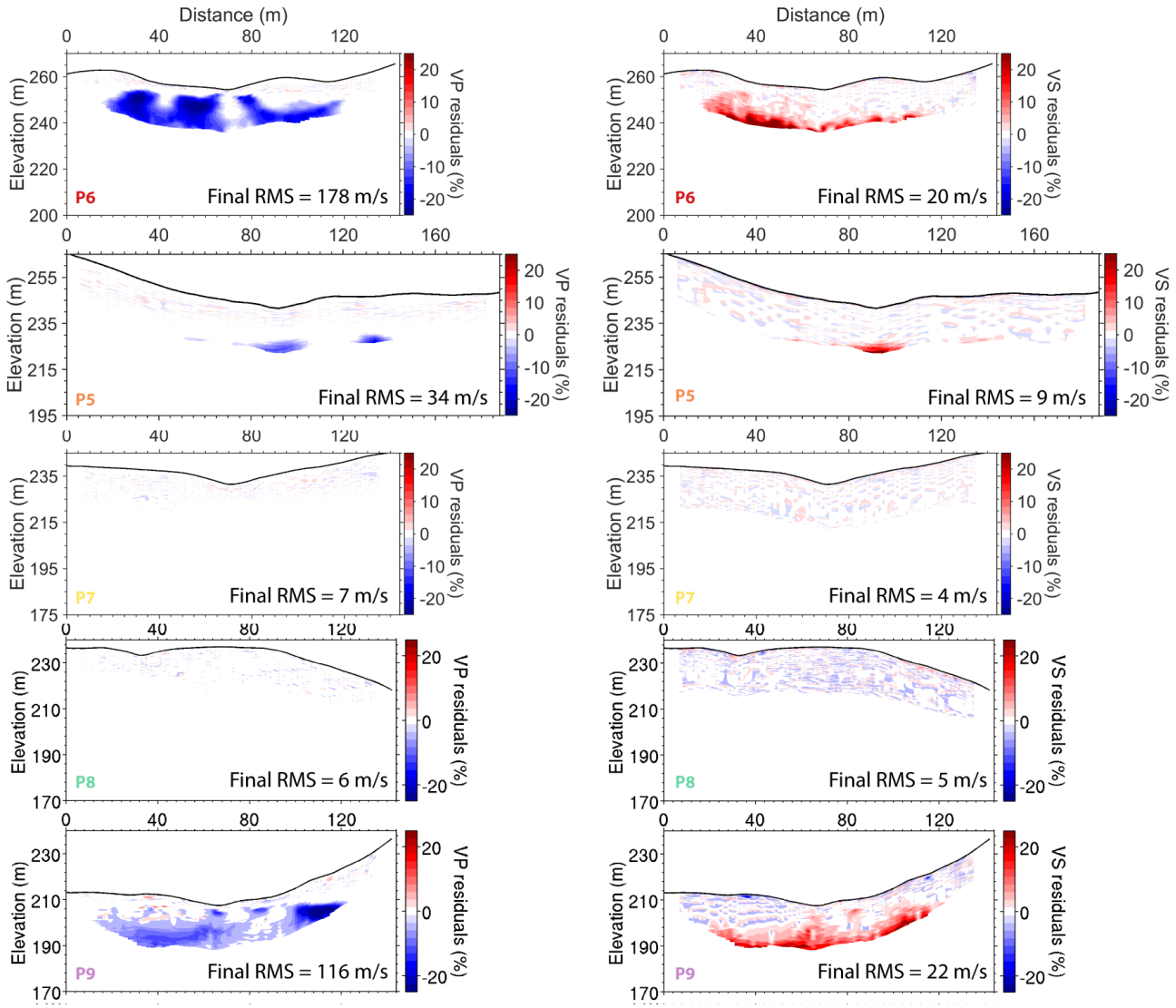

Figure S6. Velocity residuals after the grid search inversion.

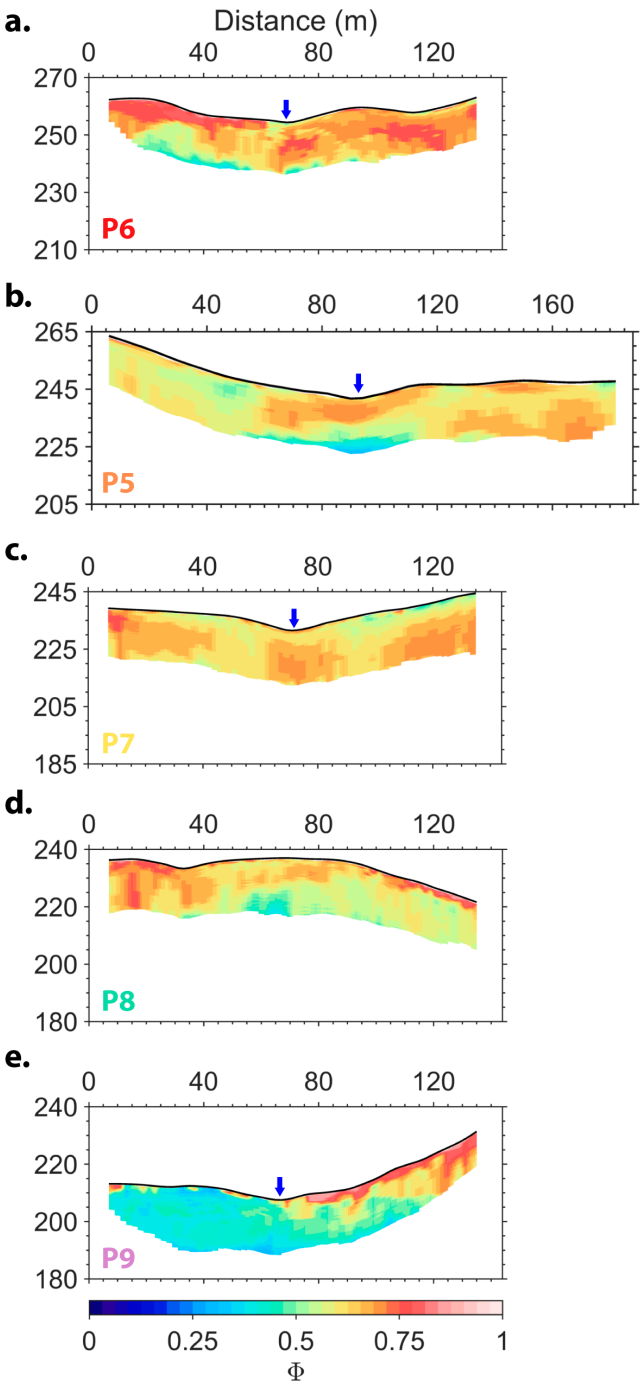

Figure S7. Porosity cross-sections obtained after the grid search inversion.

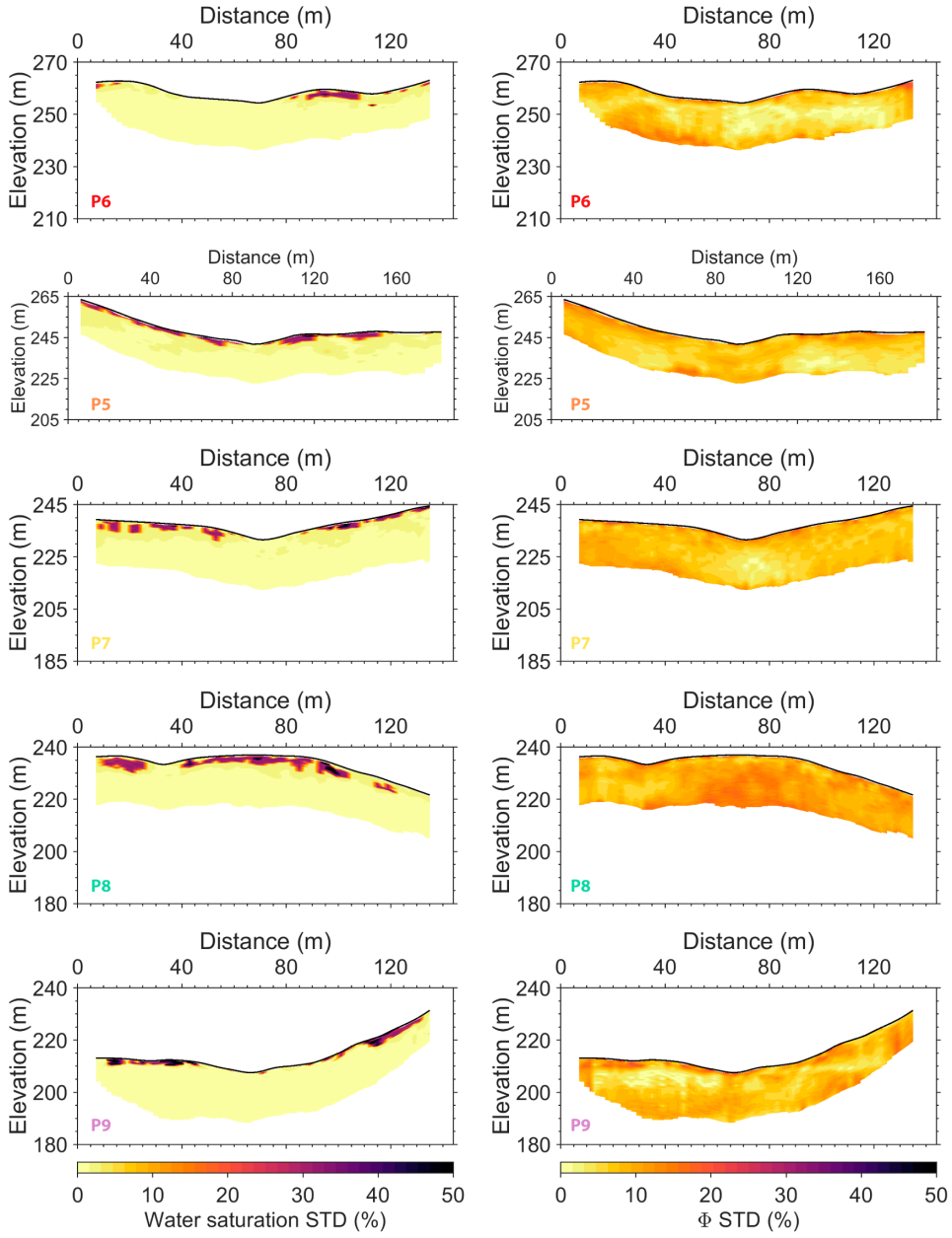

Figure S8. Porosity and saturation uncertainties estimated with the grid search inversion.

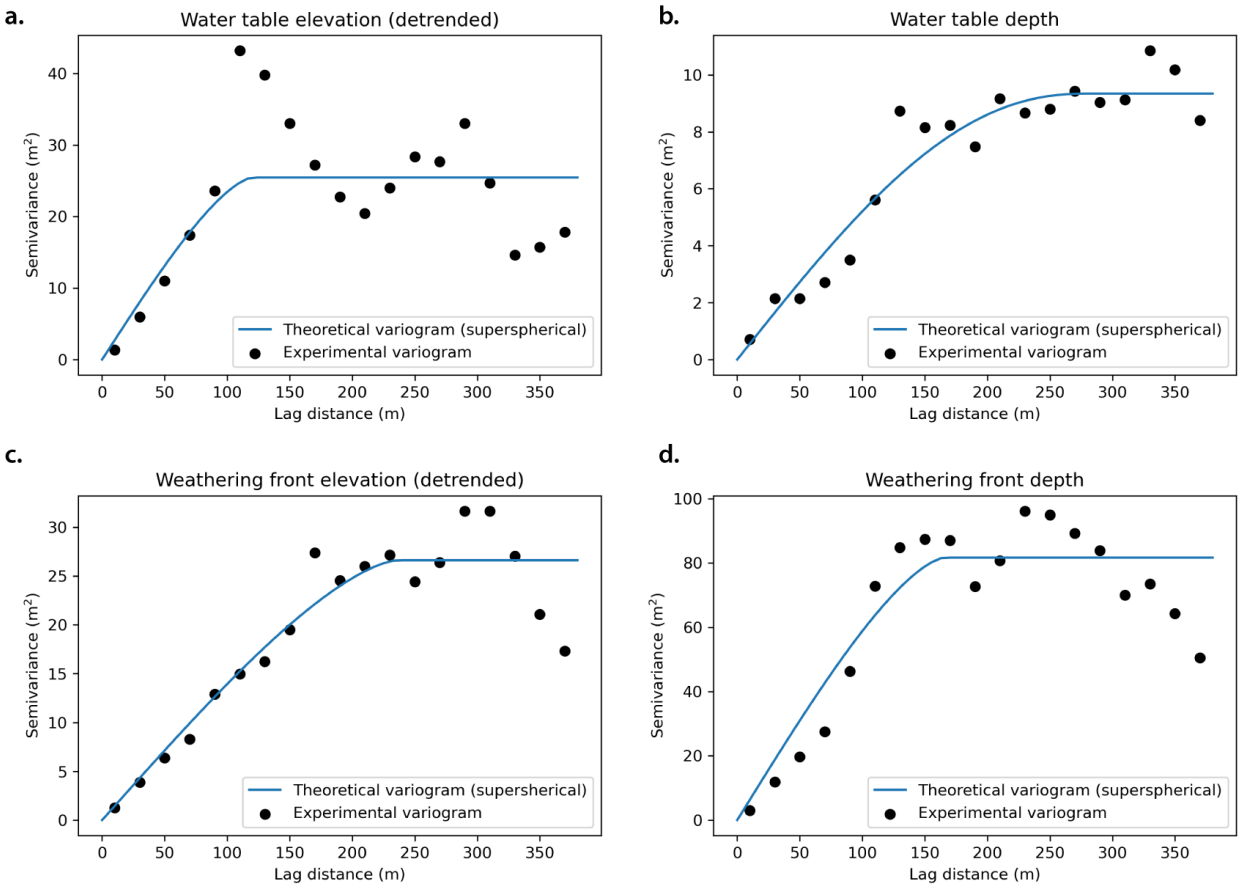

Figure S9. Experimental and theoretical variograms used for interpolating the water table (a) elevation and (b) depth. Experimental and theoretical variograms used for interpolating the weathering front (c) elevation and (d) depth.

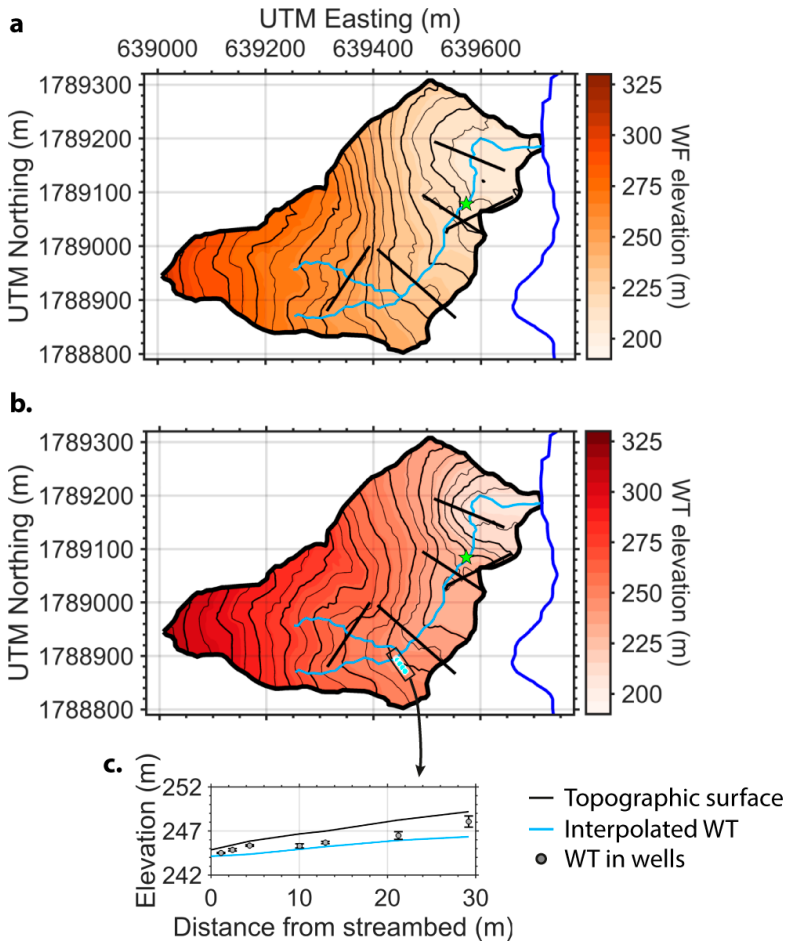

Figure S10. (a) Estimated weathering front (WF) elevation. (b) Estimated water table (WT) elevation. a-b are overlaid with 5-m elevation/depth contours. The extent of the catchment and the seismic lines are shown in black, and the hydrological network in blue. Estimated water table elevations (c) are compared with the mean values observed in the piezometric wells (light blue dots in b) during the geophysical campaign.

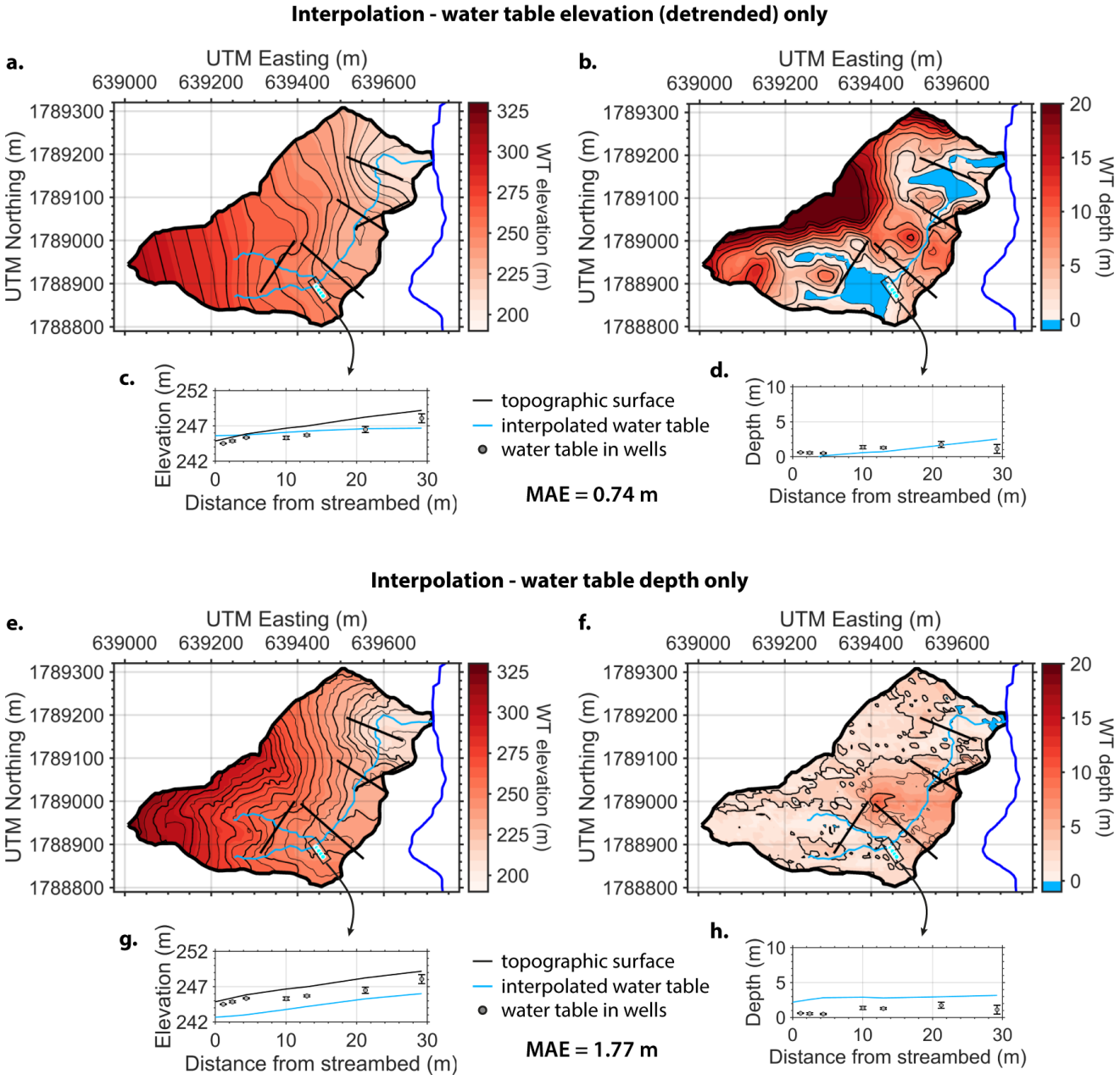

Figure S11. Water table elevation and depth obtained by interpolating detrended water table elevation only (top) and water table depth only (bottom).